ChemPubSoc Europe

DOI: 10.1002/cctc.201300181

Microstructure of Bimetallic Pt–Pd Catalysts under Oxidizing Conditions

Tyne R. Johns,[a] Jason R. Gaudet,[a, e] Eric J. Peterson,[a] Jeffrey T. Miller,[b] Eric A. Stach,[c] Chang H. Kim,[d] Michael P. Balogh,[d] and Abhaya K. Datye*[a]

Diesel oxidation catalysts (DOCs), which decrease the amount of harmful carbon monoxide (CO), nitrogen oxide (NO), and hydrocarbon (HC) emissions in engine exhaust, typically utilize Pt and Pd in the active phase. There is universal agreement that the addition of Pd improves both the catalytic performance and the durability of Pt catalysts. However, the mechanisms by which Pd improves the performance of Pt are less clear. Because these catalysts operate under oxidizing conditions, it is important to understand these catalysts in their working state. Herein, we report the microstructure of Pt–Pd catalysts that are aged in air at 750 °C. After 10 h of aging, EXAFS and XANES analysis show that the Pt is fully reduced but that almost 30% of the Pd species are present as an oxide. HRTEM images show no evidence of surface oxides on the metallic Pt–Pd particles. Instead, the PdO is present as a separate phase that is dispersed over the alumina support. Within the metallic particles, Pt and Pd are uniformly distributed and there is no evidence of core–shell structures. Therefore, the improved catalytic performance is likely associated with the co-existence of metallic Pt and Pd on the catalyst surface.

Introduction

Platinum and palladium constitute the active phase in diesel-oxidation catalysts (DOCs), which are used by the automotive industry.[1] Whereas the Pd-only catalyst shows poor performance in the NO-oxidation reaction, the addition of Pd to Pt has no detrimental effect on the catalytic activity for NO oxidation.[2] Instead, the addition of Pd leads to improved durability of the catalyst. On the other hand, there is a definite improvement in the catalytic performance for hydrocarbon[1a,c,3] and CO oxidation[1a,c,3a] if Pd is added to Pt. For these reasons, Pd is included in the formulation of commercial catalysts for diesel oxidation.[1] The mechanisms by which Pd improves the catalytic performance of Pt are not yet fully understood. To investigate the beneficial effect of added Pd, a detailed microstructural analysis was performed by Graham et al.[2b] on Pt and Pt–Pd/Al_2O_3. They found that Pt particles, which had diameters of about 6 nm in the as-prepared Pt/Al_2O_3 catalyst, grew to about 11 nm after aging under lean hydrothermal conditions (5% O_2 and 10% H_2O in N_2) at 500 °C. However, after aging at 750 °C, which is the more commonly used aging temperature, they found that, by using X-ray diffraction (XRD) the Pt particle size was 18 nm, whereas that of the Pt/Pd (50:50) catalyst was 15 nm. The improvement in dispersion as measured by CO chemisorption was consistent with these particle sizes, with the dispersion changing from 0.025 on the Pt-only catalyst to 0.030 on the bimetallic catalyst. This change, caused by the presence of Pd, would constitute a 20% improvement in the dispersion but would not explain the improved catalytic performance for the oxidation of hydrocarbons. A key difference is that during hydrocarbon oxidation the catalyst is operated in a net oxidizing environment; hence, it is important to investigate the nature of the Pt–Pd catalyst closer to its true working conditions.

A recent study of vehicle-aged Pt–Pd catalysts was reported by Ward et al.,[4] who used aberration-corrected scanning transmission electron microscopy (AC-STEM) to study the structure of fresh and road-aged Pt/SiO_2 and Pt–Pd/γ-Al_2O_3. They found that the majority of the aged bimetallic nanoparticles remained spherical and did not show any segregation but instead were randomly alloyed. Only about 30% became faceted core–shell particles with Pd segregation to the surface. Significant PdO formation was not observed, which was thought to be the result of PdO reduction into Pd metal in the CO/NO_x atmosphere. In comparison to the Pt-only sample, the addition

[a] T. R. Johns, Dr. J. R. Gaudet, E. J. Peterson, Prof. A. K. Datye
Department of Chemical and Nuclear Engineering
University of New Mexico
Albuquerque, NM 87131 (USA)
Fax: (+1)(505)277-1024
E-mail: datye@unm.edu

[b] Dr. J. T. Miller
Advanced Photon Source
Argonne National Laboratory
Argonne, IL 60439 (USA)

[c] Dr. E. A. Stach
Center for Functional Nanomaterials
Brookhaven National Laboratory
Upton, NY 11973 (USA)

[d] Dr. C. H. Kim, M. P. Balogh
Chemical and Materials Systems Lab
General Motors Global R&D
Warren, MI 48090 (USA)

[e] Dr. J. R. Gaudet
Current address: Department of Chemical Engineering
University of Michigan
Ann Arbor, MI 48109 (USA)

Supporting information for this article is available on the WWW under http://dx.doi.org/10.1002/cctc.201300181.

of Pd did not change the average particle size, although the authors did observe a narrower particle-size distribution on the bimetallic sample. This finding is similar to that reported by other groups.[1a, 2b] It is well-known that Pt sinters and has poor durability under oxidizing conditions.[2, 3a, 5] Adams and Graham[5a] showed that lean aging had a severe impact on NO_x trap performance because Pt sintered under oxidizing conditions.[2b] Surprisingly, the Pt particles grew to larger than 100 nm during aging at 900 °C, whereas the Pd-containing catalysts did not show such large particles. A similar finding was reported by Kallinen et al.,[1a] who found Pt particles as large as 1 micron after aging at 800 °C. These research groups suggested that a plausible role of Pd in these catalysts could be the formation of a surface oxide of Pd on the metal particles, which would decrease the emission of volatile Pt oxides. The AC-TEM images of Ward et al.[4] and Ezekoye et al.[2a] do not show any such surface oxides. However, a more sensitive technique for finding small amounts of Pd oxide is extended X-ray absorption fine structure (EXAFS) spectroscopy, because it can detect dispersed oxides as well as crystallites. Therefore, it is necessary to study the catalyst in its oxidized state, whereas most of these above-described studies only studied the microstructure of the Pt–Pd catalysts in their reduced state.[2]

An EXAFS study of Pt–Pd catalysts was reported by Morlang et al.[3a] They found that their Pt–Pd catalysts that were supported on silica-doped alumina were more stable and had higher catalytic activities than pure Pt catalysts. Based on their EXAFS results, they concluded that Pd was present as both an oxide and in its metallic form on the aged bimetallic catalysts. However, they could not conclusively identify the location of the oxide phase. It is well-known that a Pd-only catalyst is fully oxidized in the calcined and thermally aged state and that it can be fully transformed into its metallic state under reducing conditions. However, there is limited understanding of the location of Pd oxides on the bimetallic catalyst. Morlang et al.[3a] proposed two different models of where the PdO could be present in the thermally aged bimetallic catalyst. A PdO shell could surround the Pt–Pd core, which would suppress Pt diffusion and stabilize the catalyst; however, their HRTEM images did not show a PdO phase on the surface of the metallic particles and neither was such an oxide seen by Ezekoye et al.[2a] or Ward et al.[4] Alternatively, they proposed that PdO must be present on the surface of the bimetallic nanoparticles as nanocrystallites or on the support as isolated PdO crystals. However, they did not have any definitive evidence for such a structure, owing to the limited resolution of the TEM that was used for their work. A more recent study of alumina-supported bimetallic Pd–Pt catalysts for methane combustion was reported by Persson et al.[3c,d] They determined that the PdO that was present was in close proximity to the alloy.

Thus, as shown from this review of the literature, the characterization of these catalysts under oxidizing conditions is a significant challenge. Techniques such as XRD and TEM work best with reduced catalysts, because the metallic phase is more ordered and provides better contrast, thus making characterization easier, whereas the oxide phase is often dispersed and disordered. These previous studies raise questions about the nature of the Pd oxide in these working catalysts, which might play a crucial role in the enhanced catalytic activity, as well as the durability. X-ray absorption spectroscopy (XAS) is the technique of choice to determine the nature of dispersed oxide species and is especially useful for determining the oxidation state of Pt and Pd. However, because XAS provides information that is averaged over the entire sample, we need to complement it with a technique that has a high spatial resolution, such as aberration-corrected TEM. Furthermore, after aging, these Pt–Pd catalysts have large particles, which are beyond the characterization ability of TEM or XAS. We need complementary methods, such as scanning electron microscopy (SEM) and XRD, to obtain information over larger length scales. Herein, we used a combination of all of these techniques to develop a comprehensive picture of working Pt–Pd catalysts that were exposed to oxidizing conditions at 750 °C in air. These are the conditions most commonly used for the aging of Pt–Pd diesel-oxidation catalysts.[1a,c, 2b,c, 3a] Herein, we studied 0.8 wt.% monometallic Pt and Pd catalysts and a 1.3 wt.% Pt–Pd catalyst (40:60 atomic ratio) on two supports, γ-alumina and La-stabilized alumina, with the latter support included because it is the most commonly used support for automotive catalysts and it allowed us to study the influence of lanthana, which is used as a stabilizer for alumina supports. The results provide an insight into the nature of the phases that are present when the catalysts are operated under oxidizing conditions.

Results and Discussion

Six catalysts were prepared: Pt/La-Al_2O_3, Pt/γ-Al_2O_3, Pd/La-Al_2O_3, Pd/γ-Al_2O_3, Pt–Pd/La-Al_2O_3, and Pt–Pd/γ-Al_2O_3. The catalysts were aged at 750 °C in air for 10 h. The catalysts in this state are referred to as aged. Then, a portion of each catalyst was reduced at 250 °C for 1 h. The catalysts in this state are referred to as aged plus reduced.

The crystal structure and size of small crystalline domains can be obtained by XRD analysis and the lattice constant helps to determine the composition of the bimetallic samples. Figure 1 shows XRD patterns of La-Al_2O_3-supported Pt–Pd, Pt, and Pd catalysts after aging in air for 750 °C, as well as that of the La-Al_2O_3 support. These patterns represent the raw data as obtained from the diffractometer without any background subtraction. To allow for a comparison between the three catalysts, the data for each catalyst were vertically offset. The bimetallic and Pt samples show a peak at the (111) position. The (111) reflection occurs at $2\theta = 39.7^\circ$ for Pt and at $2\theta = 39.9^\circ$ for Pt–Pd. The bimetallic peak is shifted to the right because the lattice constant of Pt–Pd is smaller than that of Pt, according to Vegard's Law. Notably, these air-aged samples show the presence of metallic Pt but no other oxide phases. The Pd-only catalyst shows a very broad and weak reflection, which corresponds to PdO and is slightly larger on the alumina support. This result suggests that Pd is very well-dispersed over the La-alumina support and even after 10 h of aging the peaks are so broad that we cannot quantify them by using XRD. SEM and EXAFS results (see below) confirm this observation. The results

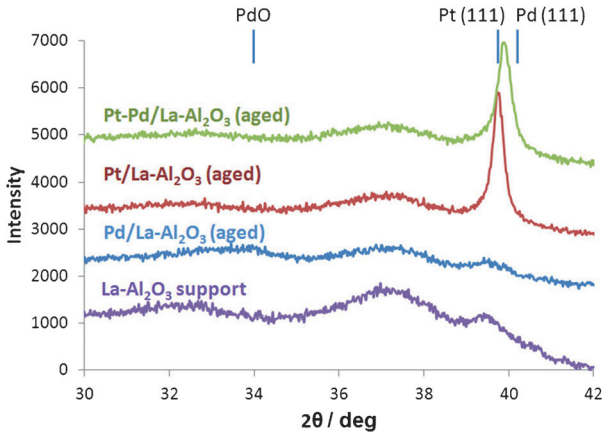

Figure 1. XRD patterns of the La-Al_2O_3 support and of Pt–Pd/La-Al_2O_3, Pt/La-Al_2O_3, and Pd/La-Al_2O_3 after aging in air at 750 °C. These patterns represent the raw data obtained from the diffractometer, without any background subtraction. To allow for a comparison between the three catalysts, the data for each catalyst are vertically offset.

Table 1. Nanoparticle sizes as determined by XRD analysis.

	Aged	Reduced	Aged	Reduced
	Pt/Al_2O_3		*Pt/La-Al_2O_3*	
Size [nm]	18.4 ± 0.4	19.6 ± 0.5	34.5 ± 0.9	34 ± 1
	Pt–Pd/Al_2O_3	*Pt–Pd/Al_2O_3*	*Pt–Pd/La-Al_2O_3*	*Pt–Pd/La-Al_2O_3*
Size [nm]	25.3 ± 0.6	22.9 ± 0.5	24.9 ± 0.7	25.8 ± 0.6
Pd/Pt composition [at.%]	32:68	32:68	32:68	32:68

for the alumina support are similar, and the XRD patterns of all of these samples are shown in the Supporting Information, Figures S-1 to S-3. Table 1 lists the average diameter of the Pt and Pt–Pd crystallites in the aged and aged-plus-reduced states on both supports. The Pt particle size is considerably larger than that of Pd because Pt is known to sinter under oxidizing conditions.[2b] Moreover, the Pt particle size is much larger on the La-modified Al_2O_3 support than on γ-Al_2O_3, thus suggesting that the presence of La is not beneficial for the dispersion of Pt. Reducing the sample in H_2 does not change any of the observed crystallite sizes, suggesting that the Pt is already fully reduced. We also do not see any metallic Pd peaks after reduction, suggesting that any metal present in its dispersed form is too small in size to be detected by XRD.

The size of the bimetallic nanoparticles was similar on both supports (approximately 25 nm), as shown in Table 1. The size of the bimetallic nanoparticles is larger than the size of the Pt nanoparticles on the γ-Al_2O_3 support suggesting that the addition of Pd did not help to prevent sintering. However, the average size of the La-Al_2O_3-supported Pt particles is much larger than that of the Pt–Pd/La-Al_2O_3 nanoparticles. The composition of the bimetallic nanoparticles was determined based on the lattice constant accounting for its deviation from ideality in a Pt–Pd alloy.[6] In our analysis, the lattice constant used for Pd was 3.890 Å. By using Rietveld refinement in GSAS, Pt was refined to 3.923 Å and the bimetallic was refined to a lattice constant of 3.909 Å. The inferred composition of the bimetallic samples, based on this lattice constant, was 32 at.% Pd and 68 at.% Pt. The reason this composition is different from the overall composition of the catalyst is that XRD only takes into account the large metallic nanoparticles. A similar discrepancy was observed by Ezekoye et al.,[2a] who found that the metallic particles were Pt-rich. We show below that the composition of the large bimetallic particles by EDS analysis agrees with the XRD analysis, because a dispersed Pd phase accounts for the balance of the Pd. The dispersed Pd species do not show up in XRD analysis.

The local molecular structure of a specific element in a sample can be inferred by EXAFS. X-ray absorption near-edge structure (XANES) analysis provides information on the coordination geometry and valence state. If aged in air, the Pd-only samples are fully oxidized, whereas, in the case of the bimetallic samples, only a portion of the Pd (20–30%) is present as an oxide (Figure 2a). Table 2 summarizes the extent of oxidation in these samples. XANES analysis was performed on catalysts on both supports; however, only the alumina-supported catalysts in the XANES figures are shown for clarity (for the remaining data, see the Supporting Information). There was very little difference between the two supports. When these samples were reduced in H_2 at 250 °C for 1 h, the Pd was fully reduced (Figure 2b). In contrast, the Pt catalysts that were aged in air were already fully reduced (Figure 3a). Further reduction in H_2 did not change either the XANES (Figure 3b) or XRD results (Figure 4).

Table 2. Oxide content of the catalysts as determined by XANES.

	Oxide content [%]	
	Aged	Aged plus reduced
Pd oxide		
Pd/Al_2O_3	100	0
Pd/La-Al_2O_3	100	0
Pt–Pd/Al_2O_3	30	0
Pt–Pd/La-Al_2O_3	20	0
Pt oxide		
Pt/Al_2O_3	0	0
Pt/La-Al_2O_3	0	0
Pt–Pd/Al_2O_3	0	0
Pt–Pd/La-Al_2O_3	0	0

Figure 5a,b shows the EXAFS Pd K-edge results for the aged and aged-plus-reduced samples, respectively. EXAFS analysis was performed on all of the catalysts that were supported on alumina and La-alumina and both supports showed similar spectra. Only the EXAFS data for the La-alumina-supported catalysts are shown for clarity. The remaining EXAFS data for all of the supports are shown in the Supporting Information. The monometallic Pd samples are both completely oxidized in the aged catalyst. The second-shell Pd–O–Pd shows decreased intensity at 3 Å, indicating the presence of very small oxide nanoparticles. The bimetallic spectra show a coexistence of PdO and the Pt–Pd alloy in the aged sample. After reduction in H_2, the Pd-only samples become metallic on both supports.

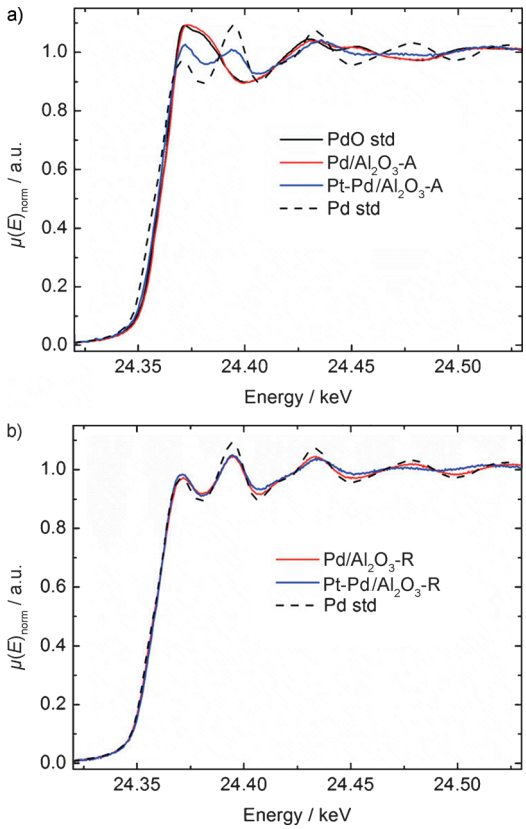

Figure 2. a) XANES plot at the Pd edge, which shows that the Pd-only catalysts are fully oxidized, whereas the bimetallic particles show that Pd is partly oxidized, even after aging at 750 °C in air for 10 h. b) XANES plot at the Pd edge after reduction in H_2, showing that the Pd is almost fully reduced in all catalysts. μ = linear absorption coefficient; A = aged, R = aged-plus-reduced sample; std = reference spectrum for bulk phase (Pd or PdO).

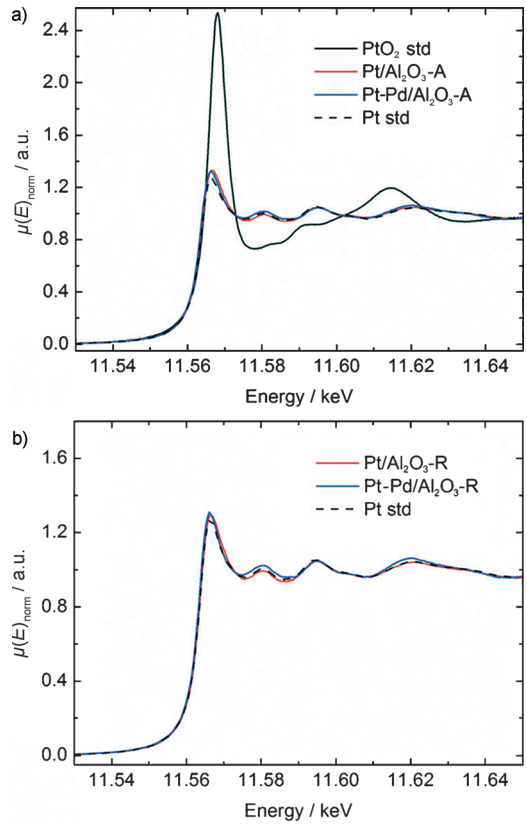

Figure 3. a) XANES plot at the Pt edge, which shows that Pt is almost fully reduced, even after aging for 10 h at 750 °C in air. b) XANES plot at the Pt edge after reduction in H_2, which shows very little change compared to the aged sample, confirming that Pt stays metallic when treated in air at 750 °C.

The coordination numbers are averaged over bulk and surface atoms; a bulk coordination number is 12. For large particles, the surface-to-volume ratio is negligible and the average value is 12. Coordination numbers of approximately 10, as shown in Table 3, indicate the presence of small particles. This result makes sense because XRD did not show any Pd peaks and in low-loading catalysts the peak broadening makes it difficult to detect a highly dispersed phase by XRD. Table 3 shows the first-shell coordination numbers for the aged and aged-plus-reduced monometallic samples that were used in this study. The uncertainty in the coordination number (N) is ±10%. For the Pd samples, the Pd–Pd coordination number represents the average number of nearest Pd neighbors and Pd–O represents the average number of nearest oxygen neighbors that surround each Pd atom. By using a similar approach, the coordination numbers are derived from the absorption at the Pt edge, thus revealing the neighbors that surround each Pt atom (Pt–Pt and Pt–O). It is clear from the coordination numbers in the table that the monometallic Pd samples have a higher dispersion than the Pt samples. The Pt coordination number of 12 in the monometallic samples indicates the presence of large metallic particles, which is consistent with the large peaks as seen by XRD and the absence of an XRD peak for the monometallic Pd sample.

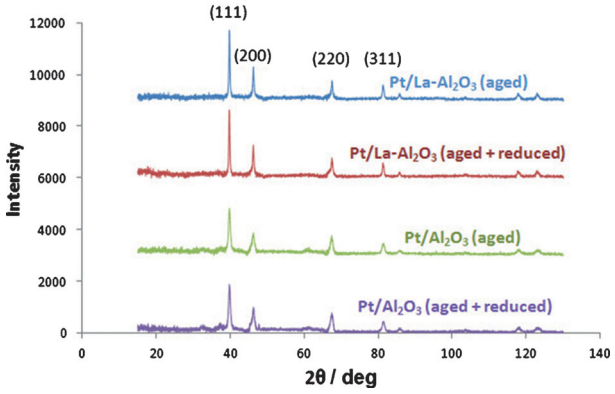

Figure 4. XRD patterns of aged and aged-plus-reduced Pt catalysts after background subtraction. To allow for a comparison between the catalysts, the data for each catalyst are vertically offset by 3000 counts.

Fourier transforms on the Pd K edge of the bimetallic samples in Figure 5 b are indicative of both Pd–Pd and Pd–Pt contributions. In the aged bimetallic catalysts, there is a metallic Pt–Pd phase, as well as a PdO phase. After reduction, there is no PdO left and there are more Pd–Pd neighbors (for the coordination numbers, see Table 4). The increase in Pd–Pd neighbors on the aged-plus-reduced catalysts likely indicates a sepa-

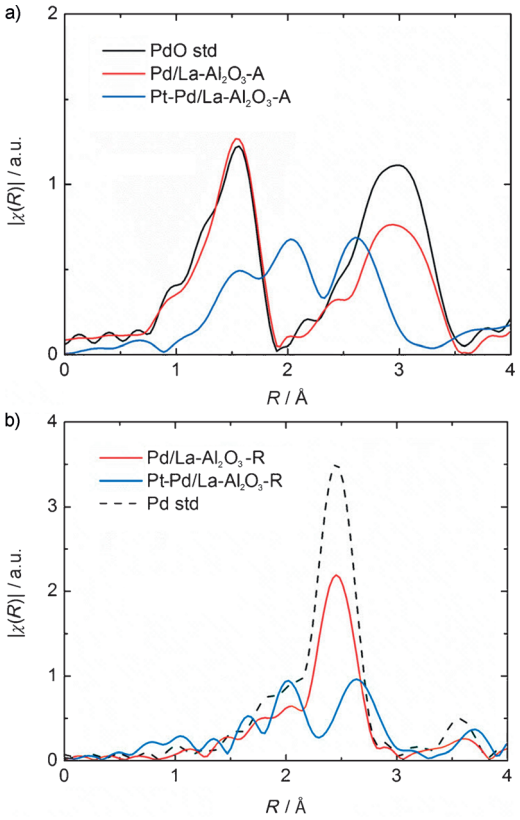

Figure 5. a) Fourier-transform EXAFS Pd K-edge results for the aged samples. The monometallic samples show peaks that correspond to Pd–O and second-shell Pd–Pd. The smaller amplitude for the second shell is consistent with the presence of small PdO species that are dispersed over the surface of the catalyst. In contrast, the bimetallic sample shows peaks that are consistent with Pt and Pd neighbors for metallic Pd and only first-shell oxide, thus suggesting that the oxide is a dispersed phase. b) EXAFS Pd K-edge results for the aged-plus-reduced samples. The monometallic samples show a Pd–Pd peak with no higher-level shells, consistent with small metal particles (which cannot be seen in XRD). The bimetallic particles show co-existence of the alloy with some dispersed Pd over the catalyst, as also confirmed by STEM-EDS analysis. χ = Magnitude of the radial form of the EXAFS equation.

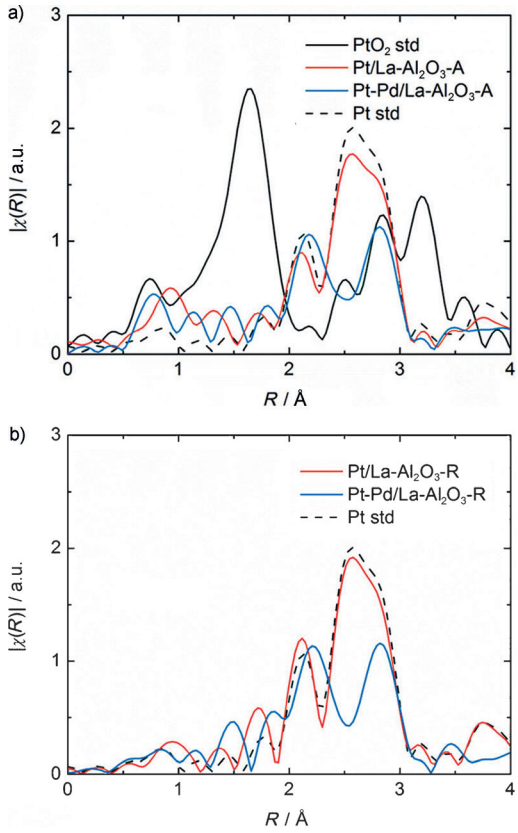

Figure 6. EXAFS Pt L3-edge results for the a) aged and b) aged-plus-reduced samples, which show very little difference between the two samples.

Table 3. EXAFS and XANES data for the monometallic samples.

Sample	Treatment	XANES fit Pd^{II} [Pt^{II}]	XANES fit Pd^{0} [Pt^{0}]	Scatter	*N*	*R* [Å]	$\Delta\sigma^{2}$ [a] [$\times10^{3}$]	ΔE_0 [b] [eV]
Pd edge								
Pd/Al_2O_3	aged	1.0	–	Pd–O	4.4	2.02	−0.8	0.7
				Pd–Pd	0.0	–	–	–
	aged plus reduced	–	1.0	Pd–O	0.0	–	–	–
				Pd–Pd	9.4	2.74	1.0	−0.5
$Pd/La\text{-}Al_2O_3$	aged	1.0	–	Pd–O	4.5	2.02	−0.6	0.6
				Pd–Pd	0.0	–	–	–
	aged plus reduced	–	1.0	Pd–O	0.0	–	–	–
				Pd–Pd	10	2.74	1.0	−0.6
Pt edge								
Pt/Al_2O_3	aged	–	1.0	Pt–O	0.0	–	–	–
				Pt–Pt	11.7	2.76	0.7	−0.4
	aged plus reduced	–	1.0	Pt–O	0.0	–	–	–
				Pt–Pt	11.6	2.76	0.2	−0.1
$Pt/La\text{-}Al_2O_3$	aged	–	1.0	Pt–O	0.0	–	–	–
				Pt–Pt	12	2.76	0.6	−0.5
	aged plus reduced	–	1.0	Pt–O	0.0	–	–	–
				Pt–Pt	11.2	2.76	−0.2	−0.3

[a] Change in the Debye–Waller factor with respect to the standard. [b] Change in edge energy relative to the standard.

rate PdO phase, which becomes metallic after the reduction treatment. Had this PdO phase been present on the surface of the bimetallic particles, one would have expected changes in Pd–Pt coordination after reduction, but the change is minor.

Figure 6a,b shows the EXAFS Pt L3-edge results. Figure 6a shows virtually no oxide on any aged catalysts from the Pt-edge analysis. The aged bimetallic samples show Pt–Pd and Pt–Pt contributions, owing to the alloyed nanoparticles. The aged-plus-reduced Pt samples, as shown in Figure 6b, are metallic on both the γ-Al_2O_3 and $La\text{-}Al_2O_3$ supports. The coordination numbers indicate large bulk-like particles, consistent with the sizes as determined by XRD. Again, the Fourier transforms of the bimetallic Pt–Pd aged-plus-reduced samples are indicative of Pt–Pt and Pt–Pd contributions. On the Pt edge, no change was caused by the reduction. The metallic particles remained the same. The reduction only turned the dispersed PdO phase into small metallic Pd nanoparticles on the bimetallic catalysts.

Table 4 lists the coordination numbers for the bimetallic samples used in this study, including the average number of nearest neighbors surrounding each atom on the Pd (Pd–O, Pd–Pd, and Pd–Pt) and Pt edges (Pt–Pt and Pt–Pd). The total coordination number gives us an idea of the size of the particles. This number is about 12 for the reduced sample,

Table 4. EXAFS and XANES data for the bimetallic samples.

Sample	Treatment	XANES fit Pd^{II} [Pt^{II}]	XANES fit Pd^0 [Pt^0]	Scatter	N	R [Å]	$\Delta\sigma^2$ [$\times10^3$]	ΔE_0 [eV]
Pd edge								
Pt–Pd/Al_2O_3	aged	0.30	0.70	Pd–O	1.7	2.05	0.0	0.5
				Pd–Pd	3.1	2.75	0.0	−2.4
				Pd–Pt	5.2	2.76	0.0	−1.3
	aged plus reduced	–	1.0	Pd–Pd	4.8	2.75	0.0	−3.0
				Pd–Pt	6.0	2.76	0.0	−3.3
Pt–Pd/La-Al_2O_3	aged	0.20	0.80	Pd–O	1.3	2.05	0.0	1.1
				Pd–Pd	3.5	2.75	0.0	−1.8
				Pd–Pt	6.8	2.76	0.0	−1.8
	aged plus reduced	–	1.0	Pd–Pd	4.6	2.75	0.0	−1.1
				Pd–Pt	7.3	2.76	0.0	−0.9
Pt edge								
Pt–Pd/Al_2O_3	aged	–	1.0	Pt–Pt	7.0	2.77	0.0	0.3
				Pt–Pd	4.5	2.76	0.0	6.8
	aged plus reduced	–	1.0	Pt–Pt	7.0	2.77	0.0	0.5
				Pt–Pd	4.6	2.76	0.0	6.8
Pt–Pd/La-Al_2O_3	aged	–	1.0	Pt–Pt	7.3	2.77	0.0	0.3
				Pt–Pd	3.5	2.76	0.0	6.8
	aged plus reduced	–	1.0	Pt–Pt	7.6	2.77	0.0	0.6
				Pt–Pd	4.0	2.76	0.0	6.3

consistent with the large particles as shown by XRD and STEM analysis. The distribution of Pt and Pd within the nanoparticles in the reduced state can be inferred from the numbers of nearest neighbors. Pt sees about seven Pt nearest neighbors and four Pd nearest neighbors and, correspondingly, Pd sees seven Pt nearest neighbors and four Pd neighbors. The uncertainty in the coordination numbers is 10%. The similarity between the coordination numbers on the Pt and Pd edges suggests that the nanoparticles have a Pt-rich and uniform (i.e., not core–shell) composition. This agreement between the coordination numbers for the Pt and Pd edges is not seen in the oxidized state of the sample. First, we see a lower total coordination number of metal atoms for the Pd edge compared to the Pt edge. We can explain this result in terms of the presence of Pd oxide. Because some of the Pd atoms see O neighbors, a smaller total number of Pd and Pt atoms are present as neighbors. There is very little change in the coordination that is seen on the Pt edge after the sample is reduced. If Pd is present as an oxide on the surface of the bimetallic particles, we would expect some change in the coordination on the Pt edge. A change is only seen on the Pd edge, thus leading us to suggest that the Pd is present as a separate phase, which is reduced in H_2 and then the number of neighboring metal atoms on average is increased for each Pd atom. The STEM/EDS results help us to corroborate the model proposed here.

STEM images were acquired on aged-plus-reduced Pt, Pd, and Pt–Pd samples supported on La-stabilized alumina to help us determine particle-size distributions. The average particle size of the Pd nanoparticles in the monometallic sample was 5.4 nm, which agreed with the low Pd–Pd coordination as seen by EXAFS. This is also why very few large particles are visible by SEM (Figure 7b). Most of the Pd is well-dispersed and consistent with the stability of Pd to sintering when treated in oxidizing atmospheres. SEM backscattered electron images did not show many Pd particles on either support. However, on the monometallic Pt sample (Figure 7c), the SEM image shows many large particles, which would explain the larger average size of 34 nm as found by XRD and an EXAFS coordination number of almost 12. The aged-plus-reduced Pt–Pd/La-Al_2O_3 catalyst had a bimodal distribution in the particle sizes. Figure 8a, b shows STEM images at different magnifications, which illustrate the different particle sizes throughout the sample. Figure 8c shows the particle-size distribution for this sample. Owing to the bimodal size distribution, we divided the particles into two groups, that is, particles smaller than 1 nm and those larger than 1 nm. The number-average, surface-average, and volume-average diameters for group of nanoparticles less than 1 nm were 0.67, 0.74, and 0.77 nm, respectively. The number-average, surface-average, and volume-average diameters for the group of particles greater than 1 nm were 16.4, 24.4, and 31.1 nm, respectively. The latter value compares favorably with the XRD-derived diameter of 25 nm (which must be multiplied by 4/3 to derive the equivalent diameter for a spherical particle).[7] Figure 7d shows an SEM image of aged-plus-reduced Pt–Pd/La-Al_2O_3. The particle sizes are similar to the particle sizes found by TEM and XRD. The overall composition of the bimetallic Pt–Pd sample was 38 at.% Pt and 62 at.% Pd, as determined by EDS. As shown below, the average composition of the larger metallic particles was Pt-rich, as also seen from the EXAFS coordination numbers.

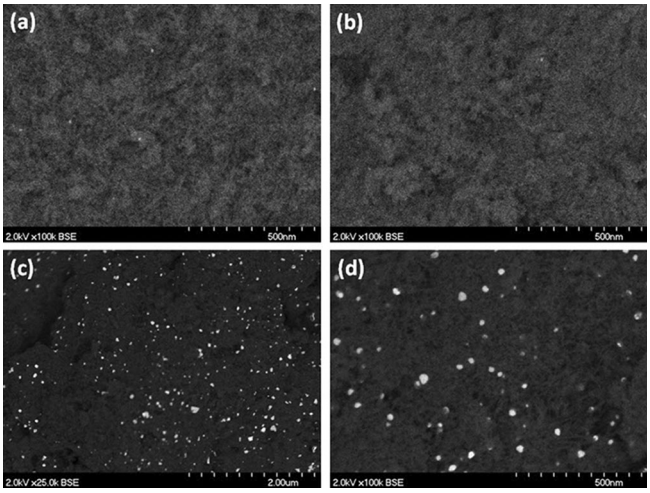

Figure 7. SEM back-scattered electron images of aged-plus-reduced a) Pd/γ-Al_2O_3, b) Pd/La-Al_2O_3, c) Pt/La-Al_2O_3, and d) Pt–Pd/La-Al_2O_3 samples. Image c was recorded at four-times-lower magnification than the other images because the particles were much larger and, consequently, fewer particles were present. The monometallic Pd samples show very few Pd particles because the majority of them are too small to see by SEM. Scale bars = 500 nm (a, b, d) and 2 μm (c).

It was important to identify the PdO phase in the bimetallic catalyst to help us explain the observed EXAFS coordination

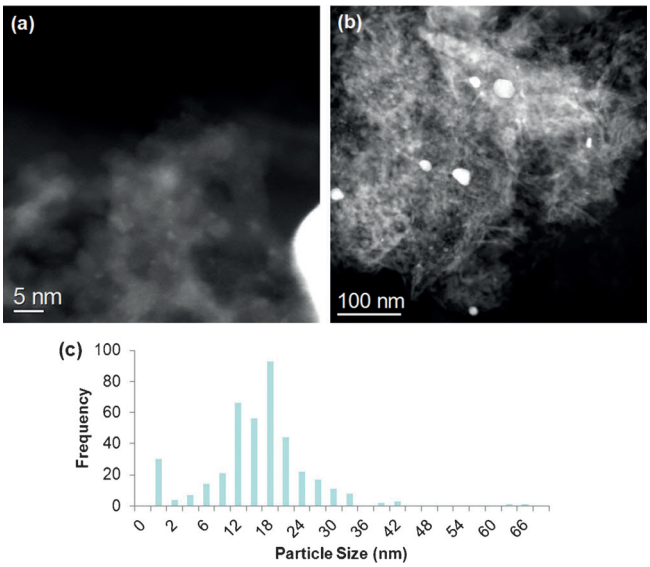

Figure 8. STEM image of a) the dispersed phase and b) large particles in the aged-plus-reduced Pt–Pd/La-Al_2O_3 catalyst; c) particle-size distribution.

numbers and the discrepancy between the overall EDS analysis and the analysis of larger metallic particles. Oxford INCA software was used to acquire EDS maps and a spectrum image was obtained that had a spectrum associated with each pixel in the image. Then, specific regions of the sample could be chosen and a spectrum was derived for all the pixels within the chosen regions. Figure 9 shows a typical image of the bimetallic reduced sample. It contains six nanoparticles with diameters of greater than 20 nm. Each particle has a box around it to indicate that the composition is determined for each of those boxed regions. The mapping software assigns colors based on the abundance of a specific element. Pd is shown in red and Pt is shown in green. A sum spectrum was obtained to determine the composition of the entire imaged region. Then, the residual composition was derived by subtracting the spectra of the six particles from the sum spectrum. By using

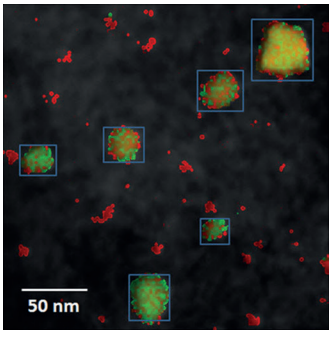

Figure 9. AC-STEM image of aged-plus-reduced Pt–Pd/La-Al_2O_3 with superimposed results from EDS mapping, in which Pt is shown in green and Pd in red. The boxes indicate the nanoparticles that contain Pt and Pd, and there is a dispersed phase, which is brighter than the surrounding support. EDS mapping allowed us to derive the average composition of the particles within the boxes, as well as in the dispersed phase, which primarily contained Pd.

this method, we found that the residual area had a Pd composition of 72 at.%, suggesting that the dispersed phase was Pd-rich. This explains the low Pd–Pd coordination obtained by EXAFS. If Pd were uniformly distributed throughout the sample in the large particles, as well as the particles of sizes of about 1 nm, the compositions would be similar to the overall average. Instead, we found that the larger particles were Pt-rich and that the dispersed phase was Pd-rich.

To understand the structure of individual nanoparticles, spot EDS was performed on specific regions of a single particle. Figure 10 shows two of the particles that were analyzed. The boxes denote the regions from which EDS spectra were obtained, and the corresponding atomic percentages of Pt and

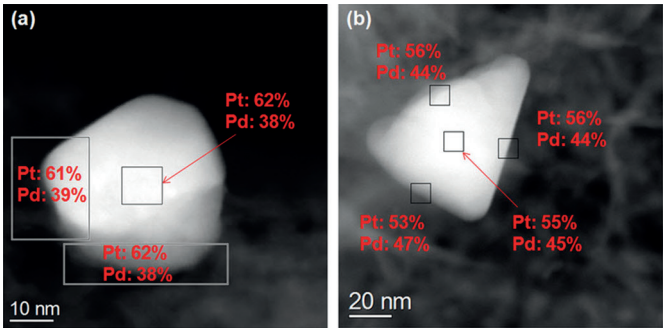

Figure 10. STEM images of two Pt–Pd particles in the aged-plus-reduced catalyst supported on La-Al_2O_3, which show the regions in which EDS was performed and the corresponding atomic percentages of Pt and Pd.

Pd are provided. High-resolution compositional mapping was performed on a JEOL JEM 2100F AC and EDS mapping allowed us to obtain average compositions of the near-surface region, as well as the entire nanoparticles. There was no evidence for a core–shell structure in any of the particles that were analyzed. There seems to be slight segregation of Pd to the surface of the nanoparticles. However, the large bimetallic nanoparticles were always rich in Pt, consistent with the composition calculated from XRD.

These results show that the monometallic Pd catalysts are well-dispersed in both the aged and aged-plus-reduced states. The sintering of Pd nanoparticles was not very pronounced during the treatment in air at 750 °C. As shown previously by ourselves,[8] the sintering of Pd becomes significantly enhanced upon heating at 900 °C, in particular with 10% H_2O, because PdO decomposes to form metallic Pd, which sinters much faster than PdO. In contrast, Pt sinters quite rapidly on aging at elevated temperatures under oxidizing conditions and the sintering of Pt is more pronounced, leading to larger particles on the La-Al_2O_3 support. Similar rates of sintering were seen on the Pt–Pd catalysts. Compared to the Pt/γ-Al_2O_3 catalyst, Pd only had a minimal effect on the final particle size; however, compared to Pt/La-Al_2O_3, Pd slowed the rate of sintering, thus yielding smaller particles in the final aged catalyst. The STEM/EDS results also show that the bimetallic sample shows a pronounced bimodal particle-size distribution, with a highly dispersed Pd-rich phase that contains particles with diameters of

about 1 nm and larger Pt–Pd particles that are Pt rich. Figure 11 shows a schematic representation of the microstructure of the catalysts after aging and subsequent reduction. We carefully probed the internal structure of the bimetallic nanoparticles and did not find any evidence of a core–shell structure nor any pronounced segregation of Pd to the surface. Core–shell Pt–Pd structures can be prepared through colloidal routes;[9] however, our aging in air may change the morphology and, therefore, the core–shell structures cannot help to explain the enhanced performance of the automotive bimetallic catalysts. If the nanoparticles had been covered by a layer of Pd, they would have behaved very differently because the Pd could transform into PdO. Our catalyst aging was performed under isothermal conditions at 750 °C in air, but the aged catalyst did not show any surface PdO on the bimetallic Pt–Pd particles, as shown in the HRTEM image in Figure 12. However, we performed our studies without the presence of water vapor and without the other constituents of automotive exhaust. Hence, further work is needed to extend the study to more realistic exhaust treatment conditions.

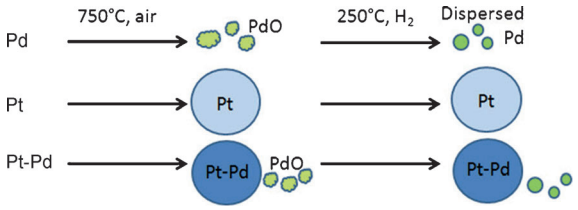

Figure 11. Schematic representation of the evolution of aged and aged-plus-reduced Pt, Pd, and bimetallic Pt–Pd particles. Aging in air causes Pd to form an oxide, but the particle size stays small. The reduced catalyst only shows small Pd particles. The Pt grows in size during aging, but stays metallic. The bimetallic nanoparticles also grow in size and both Pt and Pd stay metallic in the form of large particles (about 25 nm in diameter). There is also a dispersed Pd phase that can be seen by STEM/EDS and the presence of which is confirmed by EXAFS and XANES.

Conclusions

STEM/EDS, XRD, SEM, and XAS were used to explore the microstructure of bimetallic nanoparticles that were aged in air at 750 °C for 10 h. Our objectives were to study the influence of lanthana, which is used as a stabilizer for alumina supports, and to study the improvement in catalyst durability owing to the addition of Pd to Pt. We found that La-Al_2O_3 had a detrimental influence on the sintering of the Pt-only catalysts; however, it was beneficial for the dispersion of PdO, as seen in the slightly larger PdO XRD peak on alumina compared to that on La-alumina (see the Supporting Information, Figure S-2). With regard to durability, we found that the Pt–Pd particle sizes were between those of Pt on alumina and Pt on La-alumina. This result suggests that the improvement in particle size or dispersion owing to the added Pd is not very significant. Literature reports have shown that the addition of Pd only makes a significant difference for samples that have been aged at temperatures of 800 °C or above,[1a,2b,c] because it prevents the formation of anomalously large particles. At these temperatures, the Pd-containing catalysts had almost twice the dispersion of the Pt-only catalysts, whereas after lower-temperature aging, the difference was not as pronounced. The engine-aged bimetallic samples studied by Ward et al.[4] showed comparable mean particle sizes to Pt-only catalysts. We conclude that after aging at 750 °C in air for 10 h, the improvement in durability was not significant.

Another major objective of this study was to determine how Pd improves the catalytic behavior of Pt in the bimetallic catalysts during operation under oxidizing conditions. By using XAS, we determined that only 20–30% of the Pd in the bimetallic catalysts was present in the form of an oxide. The oxide existed as a separate phase and not as a layer on the Pt–Pd bimetallic nanoparticles, which constituted a significant difference compared to the monometallic samples (the Pd-only catalyst would consist of 100% oxide after aging under these conditions). Thus, the co-existence of Pt and Pd in metallic nanoparticles must be the key attribute of these bimetallic catalysts. There was no evidence of a core–shell structure and the extent of Pd segregation to the surface was minimal. Our results show that the surface does not become covered with an oxide, but rather any PdO exists as a separate phase. As this is a highly dispersed PdO phase, we would expect a similar phase to also be present on the monometallic Pd catalyst. Therefore, the improvement in catalytic behavior in these catalysts owes likely to a higher activity of the catalytic sites on these bimetallic particles for some of the reactions. In the oxidation of NO, this may not be very important, but for the oxidation of hydrocarbons, this difference may be significant.[1c]

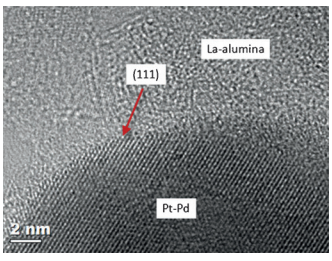

Figure 12. HRTEM image of Pt–Pd/La-Al_2O_3 that was aged at 750 °C for 10 h in air, which clearly shows no PdO on the surface of the nanoparticle.

Experimental Section

Catalyst preparation

Dispal (boehmite) was obtained from Sasol and calcined at 650 °C for 10 h to make γ-alumina, which had a BET surface area of 153 $m^2 g^{-1}$. The BET surface area was measured on a Micromeritics Gemini 2360 instrument under liquid nitrogen at 77 K. La-alumina was purchased from W. R. Grace (MI-386), contained 4 wt.% La_2O_3, and had a BET surface area of 176 $m^2 g^{-1}$. The Pt/La-Al_2O_3 and Pt/γ-Al_2O_3 catalysts were prepared by incipient wetness by using an aqueous solution of chloroplatinic acid (8 wt.% H_2PtCl_6). The Pd/γ-Al_2O_3 and Pd/La-Al_2O_3 catalyst were prepared by incipient wetness by using a 10 wt.% palladium(II) nitrate solution in 10 wt.% nitric acid. All monometallic samples had loadings of 0.8 wt.%. To syn-

thesize the bimetallic samples, tetraamine palladium(II) nitrate (10 wt.% in water) was added to the 0.8 wt.% Pt catalysts by incipient wetness to a Pt/Pd molar ratio of 40:60. This method led to a total metal loading of approximately 1.3 wt.%.

Catalyst treatments

The six samples were calcined in a box furnace at 600 °C in ambient air for 4 h. Then, each sample was reduced in a flow of 7% H_2/N_2 in a quartz tube furnace at 550 °C for 2 h. The samples were then aged in ambient air in a box furnace at 750 °C for 10 h. The catalysts in this state are referred to as "aged" (denoted as "A"). A portion of each catalyst was further reduced in 3.5% H_2/He at 250 °C for 1 h at the beamline for EXAFS experiments or in 7% H_2/N_2 for 1 h at 250 °C in the laboratory for STEM analysis. These catalysts are referred to as "aged-plus-reduced" (denoted as "R"). The BET surface area of the γ-Al_2O_3 support after these treatments was 139 $m^2 g^{-1}$ and the surface area for the La-Al_2O_3 was 172 $m^2 g^{-1}$.

XRD analysis

X-ray diffraction measurements were performed on a Rigaku SmartLab diffractometer by using CuK_α radiation. The powders were lightly pressed into a cavity in a plastic sample holder. The samples were run by using Bragg Brentano geometry with a D/tex position-sensitive detector and a NiK_β filter. The data were acquired at a rate of 16 ° min^{-1} from 15° to 130°. A step size of 0.02 was used. Diffraction peak broadening owing to instrumental effects was accounted for by using NIST standard LaB_6. All analysis was performed by using GSAS software.

STEM and EDS analyses

A JEOL 2010F 200 kV FASTEM FEG (field emission gun) TEM/STEM was used to acquire the STEM images. It had a GATAN GIF 2000 Energy Filter, JEOL bright- and dark-field STEM detectors, GATAN bright- and dark-field STEM detectors, and an Oxford Instruments ISIS/INCA EDS system with an Oxford Pentafet Ultrathin Window (UTW) Detector. Gatan Digital Micrograph was used for all image processing, and INCA was used for analysis of the EDS data. Pt and Pd L lines were used in the EDS analysis. This microscope has a point-to-point resolution of 0.194 nm and a minimum spot size in STEM mode of 0.14 nm. However, for the compositional analysis by using EDS, we used a probe size of 1.0 nm to obtain adequate counting statistics. For high-resolution compositional mapping, we also used a JEOL JEM 2100F AC (aberration-corrected STEM). The nominal point resolution and ultimate probe size for this instrument were similar to those of the JEOL 2010F, but the aberration corrector provided a much higher probe current for EDS analysis. The microscope was configured for both traditional TEM and STEM. Images for this work were recorded by using a high-angle annular dark field (HAADF) detector. The electron source on this microscope was a field-emission gun and the microscope was equipped with a STEM mode spherical aberration corrector (Cs).

High-resolution TEM (HRTEM) images were recorded on an FEI Titan 80–300 environmental transmission electron microscope (E-TEM) at the Center for Functional Nanomaterials at Brookhaven National Laboratory. This microscope was equipped with an objective-lens aberration corrector and had a spatial resolution of 0.08 nm in HR phase contrast mode.

Scanning electron microscopy

The SEM images were recorded on a Hitachi S-5200, which was capable of a resolution of 1.7 nm at 1 kV and 0.5 nm at 30 kV. It was operated at 2 kV to image the samples in backscattered mode as well as in the secondary electron mode. The catalyst sample was prepared by pressing the powder onto double-sided carbon tape attached to the sample holder.

X-ray absorption spectroscopy (XAS)

Pd K-edge and Pt L3-edge X-ray absorption measurements were performed at RT on the insertion device beamline 10-ID-B at the Advanced Photon Source (APS) at Argonne National Laboratory in transmission mode. The amount of catalyst loaded into the sample holder was selected to obtain an edge step of 0.3–1.0 for the given experiment. Each aged catalyst was ground to a fine, uniform consistency and compressed into a stainless steel sample holder (die) with six cylindrical openings for up to six samples. The die was inserted into a quartz tube sample cell, which had an inner diameter of 3/4" and X-ray transparent end caps made of Kapton. The cell allowed for the flow of gases, and it was mounted onto a movable sample stage, which allowed for sample alignment in the beam path. After XAS was completed on the aged samples, the sample cell was taken off-line to perform additional sample treatments. A flow of 50 $cm^3 min^{-1}$ of He was first delivered into the cell for 5 min to purge O_2. Then, a reducing environment of 3.5% H_2/He was provided for 1 h at 250 °C, followed by a purge of He for 5 min at the same temperature. This purge was done to prevent formation of Pd hydrides during the cool down. Then, the cell was removed from the furnace and cooled to RT under a flow of He. Once it reached RT, the sample cell was disconnected from the gas feed and sealed with He inside. Then, X-ray absorption measurements were performed on the aged-plus-reduced samples.

Linear combination fitting (LCF) of the data to both metallic and metal-oxide standards was performed to determine the oxidation state of each metal in the near-edge portion of the spectra (XANES). Analysis of the extended portion of the spectra (EXAFS) provided bond distances and the coordination of each metal, which indicated the extent of Pt–Pd alloying and particle sizes (nanoparticles versus bulk material). ATOMS[10] and FEFF6[11] software packages were used to generate ab initio photoelectron scattering models of structures that contained Pt, Pd, and O. Face-centered cubic (FCC) Pt and Pd paths were created by using data reported by Kittel.[12] Data from Waser et al.[13] were used to generate a PdO structure (space group P42/mmc; antifluorite derivative) with an origin shift of (0,1/2,0) to comply with the positions listed in the International Tables for Crystallography[14] with Pd in site 2c and O in site 2f. To account for the alloying of Pd and Pt, substitution of Pd sites with Pt (and vice versa) was used. Then, a least squares fitting algorithm was used to fit the models to the experimental EXAFS spectra, which allowed for the determination of bond distances, as well as the coordination number for the Pt and Pd absorbers.

Acknowledgements

We acknowledge financial support from the NSF through grants GOALI CBET-1067803, IGERT DGE-0504276, and PIRE OISE-0730277. Part of this work was performed at beamline 10-ID-B (MRCAT) of the Advanced Photon Source at the Argonne National

Laboratory. MRCAT operations were supported by the Department of Energy and the MRCAT member institutions. The use of the Advanced Photon Source was supported by the U.S. Department of Energy, Office of Science, Office of Basic Energy Sciences under Contract No. DE-AC02-06CH11357. J.T.M. is supported as part of the Institute for Atom-Efficient Chemical Transformations (IACT), an Energy Frontier Research Center funded by the U.S. Department of Energy, Office of Science, Office of Basic Energy Sciences. Part of this work was performed on a JEOL JEM 2100F AC at General Motors Global R&D, and some work was performed on an FEI Titan 80-300 environmental transmission electron microscope (E-TEM) at the Center for Functional Nanomaterials at Brookhaven National Laboratory, supported by the U.S. Department of Energy, Office of Basic Energy Sciences, under contract No. DE-AC02-98CH10886. We also acknowledge support from the NSF for the acquisition of the XRD through a Major Research Instrumentation grant (CBET 0960256). We thank Hien Pham for her assistance in obtaining the SEM images.

Keywords: EXAFS spectroscopy · bimetallic catalysts · palladium · platinum · structure elucidation

[1] a) K. Kallinen, A. Moreno, A. Savimäki, T.-J. J. Kinnunen in *SAE Technical Paper 2009-26-0018*, **2009**; b) T. C. Watling, M. Ahmadinejad, M. Ţuţuianu, Å. Johansson, M. A. J. Paterson, *SAE Int. J. Engines* **2012**, 5; c) C. H. Kim, M. Schmid, S. J. Schmieg, J. Tan, W. Li, *SAE Technical Paper 2011-01-1134*, **2011**.

[2] a) O. K. Ezekoye, et al., *J. Catal.* **2011**, *280*, 125 – 136; b) G. W. Graham, H. W. Jen, O. Ezekoye, R. J. Kudla, W. Chun, X. Q. Pan, R. W. McCabe, *Catal. Lett.* **2007**, *116*, 1 – 8; c) M. Kaneeda, H. Iizuka, T. Hiratsuka, N. Shinotsuka, M. Arai, *Appl. Catal. B* **2009**, *90*, 564 – 569.

[3] a) A. Morlang, U. Neuhausen, K. V. Klementiev, F. W. Schutze, G. Miehe, H. Fuess, E. S. Lox, *Appl. Catal. B* **2005**, *60*, 191 – 199; b) K. Persson, A. Ersson, S. Colussi, A. Trovarelli, S. G. Jaras, *Appl. Catal. B* **2006**, *66*, 175 – 185; c) K. Persson, A. Ersson, K. Jansson, J. L. G. Fierro, S. G. Jaras, *J. Catal.* **2006**, *243*, 14 – 24; d) K. Persson, K. Jansson, S. G. Jaras, *J. Catal.* **2007**, *245*, 401 – 414; e) K. Persson, L. D. Pfefferle, W. Schwartz, A. Ersson, S. G. Jaras, *Appl. Catal. B* **2007**, *74*, 242 – 250.

[4] M. R. Ward, T. Hyde, E. D. Boyes, P. L. Gai, *ChemCatChem* **2012**, *4*, 1622 – 1631.

[5] a) K. M. Adams, G. W. Graham, *Appl. Catal. B* **2008**, *80*, 343 – 352; b) M. Chen, L. D. Schmidt, *J. Catal.* **1979**, *56*, 198 – 218; c) G. W. Graham, H. W. Jen, W. Chun, H. P. Sun, X. Q. Pan, R. W. McCabe, *Catal. Lett.* **2004**, *93*, 129 – 134; d) S. S. Mulla, N. Chen, L. Cumaranatunge, G. E. Blau, D. Y. Zemlyanov, W. N. Delgass, W. S. Epling, F. H. Ribeiro, *J. Catal.* **2006**, *241*, 389 – 399; e) S. B. Simonsen, I. Chorkendorff, S. Dahl, M. Skoglundh, J. Sehested, S. Helveg, *J. Am. Chem. Soc.* **2010**, *132*, 7968 – 7975; f) S. B. Simonsen, I. Chorkendorff, S. Dahl, M. Skoglundh, J. Sehested, S. Helveg, *J. Catal.* **2011**, *281*, 147 – 155; g) N. L. Wu, J. Phillips, *J. Appl. Phys.* **1986**, *59*, 769 – 779; h) N. L. Wu, J. Phillips, *J. Catal.* **1988**, *113*, 129 – 143; i) Z. M. Zhou, Z. G. Shao, X. P. Qin, X. G. Chen, Z. D. Wei, B. L. Yi, *Int. J. Hydrogen Energy* **2010**, *35*, 1719 – 1726; j) D. H. Kim, Y. H. Chin, G. G. Muntean, A. Yezeretz, N. W. Currier, W. S. Epling, H. Y. Chen, H. Hess, C. H. F. Peden, *Ind. Eng. Chem. Res.* **2006**, *45*, 8815 – 8821.

[6] J. B. Darby, K. M. Myles, *Metall. Trans.* **1972**, *3*, 653 – 657.

[7] R. J. Matyi, L. H. Schwartz, J. B. Butt, *Catal. Rev. Sci. Eng.* **1987**, *29*, 41 – 99.

[8] Q. Xu, K. C. Kharas, B. J. Croley, A. K. Datye, *ChemCatChem* **2011**, *3*, 1004 – 1014.

[9] R. Esparza, A. F. García-Ruiz, J. J. Velázquez Salazar, R. Pérez, M. José-Yacamán, *J. Nanopart. Res.* **2013**, *15*.

[10] B. Ravel, *J. Synchrotron Radiat.* **2001**, *8*, 314 – 316.

[11] A. L. Ankudinov, B. Ravel, J. J. Rehr, S. D. Conradson, *Phys. Rev. B* **1998**, *58*, 7565 – 7576.

[12] C. Kittel, *Introduction to Solid State Physics, 8th ed.*, Wiley, Hoboken, **2005**.

[13] J. Waser, H. A. Levy, S. W. Peterson, *Acta Crystallogr.* **1953**, *6*, 661 – 663.

[14] *International Tables for Crystallography, Vol. A: Space Group Symmetry, 5th ed.*, Kluwer, Dordrecht, **2002**.

Received: March 13, 2013
Published online on July 2, 2013